Three-Dimensional Chiral Morphogenesis of Active Fluids

Zhong-Yi Li,* Yun-Ping Chen,* Hao-Yu Liu, and Bo Li†
Institute of Biomechanics and Medical Engineering, Applied Mechanics Laboratory, Department of Engineering Mechanics, Tsinghua University, Beijing 100084, China

(Received 26 April 2023; accepted 29 February 2024; published 25 March 2024)

Chirality is an essential nature of biological systems. However, it remains obscure how the handedness at the microscale is translated into chiral morphogenesis at the tissue level. Here, we investigate three-dimensional (3D) tissue morphogenesis using an active fluid theory invoking chirality. We show that the coordination of achiral and chiral stresses, arising from microscopic interactions and energy input of individual cells, can engender the self-organization of 3D papillary and helical structures. The achiral active stress drives the nucleation of asterlike topological defects, which initiate 3D out-of-plane budding, followed by rodlike elongation. The chiral active stress excites vortexlike topological defects, which favor the tip spheroidization and twisting of the elongated rod. These results unravel the chiral morphogenesis observed in our experiments of 3D organoids generated by human embryonic stem cells.

DOI: 10.1103/PhysRevLett.132.138401

Understanding morphogenesis of organs and organisms is central for developmental biology and has attracted considerable attention since the 1900s [1]. In the morphogenetic process, cellular activity enables collective cell motion and self-organization far beyond the individual scale, leading to diverse architectures and patterns [2–7]. The framework of active matter theory provides an elegant approach for addressing the morphodynamics emerging in these nonequilibrium systems [8–15]. Through this framework, a wealth of experimental observations including morphological transition from two-dimensional (2D) to three-dimensional (3D) [16,17] and defect-regulated morphogenesis [18–20] have been reproduced. Despite these exciting progresses, it remains incompletely understood how the active interactions at the cellular scale mediate the 3D structure formation and pattern evolution at the tissue level.

During early development, embryos undergo multiple symmetry breaking processes to establish specific organs or structures. For example, vertebrate embryos break left-right symmetry during gastrula development, thus determining the left and right axes of the body plane, which profoundly affects the localization and development of internal organs [4,21]. This process is found to be related to the chiral rotation of the cilia of the pit cells [22,23]. A chiral rotation of the cortex can also occur in the *Xenopus* embryo to identify the dorsoventral region [24,25], which is crucial for the embryo to achieve normal biological function. The left-right symmetry breaking at the tissue scale may associate with the chiral dynamics of cells. Although individual cells are known to exhibit chirality [26–28], depending on the intracellular actomyosin activity, the long-range coordination of cell chirality is yet to be explored. Recent studies have revealed many unique functions and characteristics of collective chirality emerging in multicellular tissues, including coordinated rotation [29,30], robust directional flow [31–33], and defect motion regulation [34–36]. However, most studies were focused on 2D systems, and the understanding of 3D chiral morphogenesis is limited.

Motivated by morphogenesis of organoids derived from human embryonic stem cells (hESCs), we explore the 3D self-organization of collective cells by deploying the active chiral fluid theory and simulations. We reveal that the chiral interactions of cells can be translated to the tissue level, forming 3D papillary and helical structures. We quantify the morphological characteristics and show that the chiral

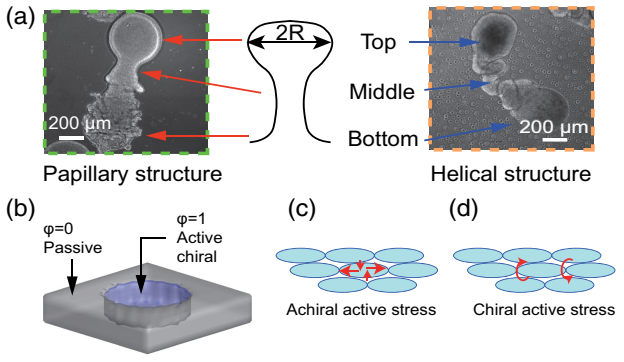

FIG. 1. Experimental observation and theoretical model setup. (a) 3D tissue morphogenesis in experiment of hESCs under different induction. Papillary structure observed at day 7 (left), helical structure observed at day 9 (right), and a morphological schematic (middle) are shown. (b) Schematic of the boundary settings in theory. (c),(d) Schematics of active stresses. The ellipses represent cells, and the red arrows represent force dipoles in (c) and moment dipole in (d).

morphologies result from the trade-off between chiral and achiral active stresses. Our results suggest a key role of chirality transmission in tissue development.

We generated matrigel-coated circular micropatterns with radius 200 μm on polydimethylsiloxane surfaces using microcontact printing [37,38]. Then hESCs were seeded on the 2D circular micropatterns. After attaching to micropatterns, cells were treated with induction medium, and 1 day later, hESCs formed 2D monolayer tissues on micropatterns (see Supplemental Material (SM) [39] for details). After 3 days, we observed that the 2D monolayer tissue on micropatterns can spontaneously bud in the vertical direction, followed by the bud elongation up to forming a 3D organoid. These organoids first exhibit a papillary architecture, with a swelling head and a thin frenulum, and then the frenulum either remains straight or undergoes twisting to form a helical structure under different induction [Fig. 1(a)] (Movies S1 and S2). We next adopt the active fluid theory to reproduce the experimentally observed organoid morphogenesis and explore the regulatory factors.

We describe the relative concentration of active and passive fluids by φ, where $\varphi = 1$ represents the active tissue and 0 denotes the passive surrounding environment. Consistent with the experimental scenario, we set a cylindrical domain on the substrate, with $\varphi = 1$ inside and $\varphi = 0$ outside the domain [Figs. 1(b) and S1]. By setting such Dirichlet boundary conditions for the cylindrical domain [18], which enables the continuous transport of active fluids from the cylindrical domain into the bulk, we can approximately simulate tissue growth. Of note, the mass increase introduced here is not exactly the same as that caused by cell proliferation. The evolution of φ is governed by [20]

$$\partial_t \varphi + \nabla \cdot (\varphi \mathbf{v}) = M \Delta \mu, \tag{1}$$

where $\mathbf{v}$ is the velocity of cells, and μ is the chemical potential, dictated by the variation of the free energy F through $\mu = \delta F / \delta \varphi$ [39]; M denotes the diffusion coefficient. Because cells commonly display end to end asymmetry in structure or protein distribution to some extent [Fig. S2], we assume the active tissue to be polar [39,40]. The polarization of cells in the active tissue is described by $\mathbf{p}$, which obeys [41]

$$\partial_t \mathbf{p} + \mathbf{v} \cdot \nabla \mathbf{p} = \lambda \mathbf{E} \cdot \mathbf{p} + \boldsymbol{\omega} \times \mathbf{p} + \Gamma \mathbf{h}, \tag{2}$$

where $\mathbf{E}$ is the strain rate, $\boldsymbol{\omega}$ is the vorticity, and λ denotes the flow alignment coefficient, which controls the alignment of cells with the flow. $\mathbf{h} = -\delta F / \delta \mathbf{p}$ is the molecular field and Γ is the rotational diffusivity coefficient. We set the cellular polarization direction at the boundary toward the center of the circular domain, which has been verified by our experimental observation [Fig. S3] and previous experiments [39,42,43]. The nonequilibrium interactions between cells can generate active motion, which leads to morphogenesis and dynamic adjustment of polarization direction. We deploy the Navier-Stokes equation to describe the collective motion of cells,

$$\rho(\partial_t \mathbf{v} + \mathbf{v} \cdot \nabla \mathbf{v}) = -\nabla p + \eta \Delta \mathbf{v} + \nabla \cdot (\boldsymbol{\sigma}_p + \boldsymbol{\sigma}_a + \boldsymbol{\sigma}_c), \tag{3}$$

where ρ is the density, assumed to be constant, which requires $\nabla \cdot \mathbf{v} = 0$; η is viscosity, and p is the pressure. The passive stress $\boldsymbol{\sigma}_p$ consists of surface tension and elastic stress due to polar elasticity [39,41,44,45]. $\boldsymbol{\sigma}_a$ and $\boldsymbol{\sigma}_c$ denote the achiral and chiral active stresses that characterize nonequilibrium interactions between cells, respectively. The achiral stress describes the active intercellular force transfer mediated by E-cadherin [46–48], that is, the force dipole outward along the long axis of the cell [Fig. 1(c)]. Its coarse-grained description is expressed as $\boldsymbol{\sigma}_a = -\zeta_a(\mathbf{pp} - |\mathbf{p}|^2 \mathbf{I}/3)$ [18,41], where ζ_a is the achiral activity coefficient and $\mathbf{I}$ is a unit tensor. The chiral stress describes the torque dipole between cells [49,50], which causes the interacting cells to counter-rotate [Fig. 1(d)]. Its coarse-grained description is expressed as $\boldsymbol{\sigma}_c = -\zeta_c \nabla \times (\mathbf{pp})$ [51,52], where ζ_c is the chiral activity coefficient. The sign of the chiral stress determines whether the system is clockwise ($\zeta_c > 0$) or counterclockwise ($\zeta_c < 0$). Here, we ignore the chiral contribution resulting from the spin of the cell around the direction $\mathbf{p}$ [51,52] because the generation of the net angular momentum has been neglected at the microscopic level.

To explore the influence of achiral and chiral active stresses on morphogenesis, Eqs. (1)–(3) are numerically solved by using a hybrid lattice Boltzmann method [51,53–55]. The emerging morphologies under different achiral and chiral activity are illustrated in a diagram [Fig. 2]. With

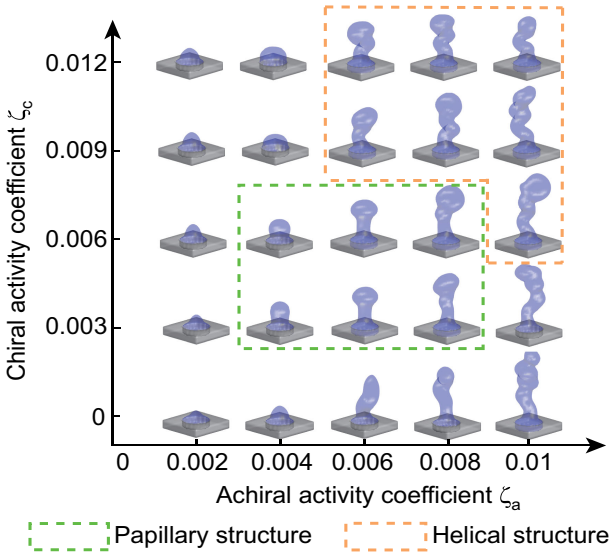

FIG. 2. Morphological diagram as the function of achiral and chiral activity (ζ_a, ζ_c). Each snapshot is taken at $t = 10000$. Green and orange box denotes the simulated papillary and helical structures, respectively.

a low achiral stress, only shallow humps can be formed (Movies S3–S5), as routinely observed in experiments of C2C12 cells [42,43]. The increased achiral stress can trigger out-of-plane budding and subsequent bud elongation, leading to a rod-shaped tentacle. The formation of rod-shaped tentacles also occurs in *Hydra* development [56,57] and self-organization of myoblasts [43]. Intriguingly, we find that under appropriate chiral stress levels, the tip of the rod-shaped tentacle will locally develop a spheroid, yielding a papillary structure with a frenulum connecting the spheroid and the bottom structure. Recent work showed that the mammary gland organoids can undergo the similar expansion at the tip to form spherical alveoli [58]. Nevertheless, the mechanisms behind them are different, since the mammary alveoli are primarily sculpted by the competition of inner pressure and surrounding collagen matrix, which are absent in our system. In addition, for a low chiral stress, the frenulum of the papillary structures is straight, while increased chirality results in twisting in the frenulum, forming a helical structure. Both papillary and helical structures were observed in our experiments under different induction conditions [Fig. 1(a)]. Besides, the appropriate size of the substrate confinement is also crucial for morphogenesis, whereas the influence of viscosity is relatively weak [Figs. S4 and S5] [39].

We next examine the salient features of the two self-organized structures by tracking their formation processes in simulations [Figs. 3(a) and 3(b)]. Under a relatively low chiral stress ($\zeta_c > 0$), the achiral activity drives the living active matter to undergo a cascade of morphological transitions from a 2D layer to a tapered hump, then to a rod-shaped tentacle, and to a papillary structure with a spheroidal head at the top, while the emerging structures maintain an elongated configuration [Fig. 3(a)] (Movie S6). At intermediate chiral activity, however, the formed rod-shaped tentacle is likely to break the axial symmetry to yield a 3D spiral structure [Fig. 3(b)] (Movie S7). To better illustrate the handedness of the spiral structure, the central helical axis $\mathbf{r}_0 = (x_0, y_0, z_0)$ is identified and the phase angle of the axis is calculated by $\arctan 2(-\Delta x_0, \Delta y_0)$, as shown in Fig. 3(c), where Δ means difference operation along the central helical axis. The phase angle gradually decreases from the tentacle bottom to the top, exhibiting a clockwise (or counterclockwise if $\zeta_c < 0$) torsion without reversal, consistent with the handedness of the prescribed chiral activity. This indicates that the chiral active stress behaves like two opposite torques applied to the upper and lower ends of the frenulum to create a clockwise helix. The polarization field $\mathbf{p}$ is nonuniform in the vertical direction and displays local distortion [Figs. 3(d) and 3(e)]. The continuous injection of active matter enables the emerging structures to grow constantly, instead of maintaining a steady configuration.

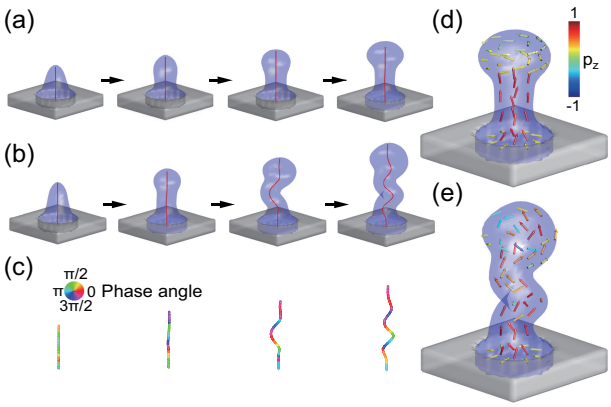

FIG. 3. Morphological features of two typical structures. (a) The snapshots of papillary structure formation when $\zeta_a = \zeta_c = 0.006$. The red curve is the central axis. (b) Snapshots of the helical structure formation when $\zeta_a = 0.008$ and $\zeta_c = 0.009$. In (a) and (b), the time points are $t = 2000$, 4000, 6000, and 9000, respectively. (c) The central axis during the helical structure formation corresponding to (b). (d),(e) Polarization fields $\mathbf{p}$ corresponding to (a) and (b). The arrows show the direction of $\mathbf{p}$, and the color denotes the magnitude of the z component p_z of $\mathbf{p}$.

We explore the mechanisms underlying morphogenesis of 3D papillary and helical structures. Three states are focused on, namely, (i) out-of-plane budding at the initial stage, (ii) spheroidization at the top, and (iii) spiralization at the middle frenulum [Fig. 4(a)]. We calculate the active forces $\mathbf{F}_a = \nabla \cdot \boldsymbol{\sigma}_a$ and $\mathbf{F}_c = \nabla \cdot \boldsymbol{\sigma}_c$ to analyze their influence on the structure formation. At the initial stage [state (i)], the polarized cells at the substrate spontaneously nucleate an asterlike +1 topological defect (green circle), where a vertically aligned core forms in the center, subsequently, inducing budding growth in the third dimension. The defect may remain stable under appropriate activity only [Fig. S6]. This self-organized structure has been proved to be essential for the 3D transformation of tissues [18,42,43,59,60]. Such asterlike +1 defect is responsible for the budding, whereas contributes little to the subsequent complex morphogenesis. Two active forces $\mathbf{F}_a$ and $\mathbf{F}_c$ are vertically upward in the center, indicating that they both drive budding and elongating, but the former dominates [Fig. 4(b); Fig. S7] (Movie S8) [39].

At the tip of the bud (orange circle), the polarization direction is basically vertical, see state (i) in Fig. 4(a). Yet, this vertical state is unstable because the interaction of torque dipoles between cells, described by chiral active stress, can push neighboring cells to rotate and then produce local twisting [49,51,52,61]. It may lead to two outcomes. On the one hand, it causes the polarized cells to twist from the vertical direction into the plane, generating a counterclockwise vortexlike +1 topological defect. We evaluate $\mathbf{F}_a$ in the polar coordinates and find that its radial component F_r is much larger than the circumferential one F_θ [Fig. 4(c)] (Movie S8), which indicates that $\mathbf{F}_a$ is radially outward and thus able to drive the local expansion

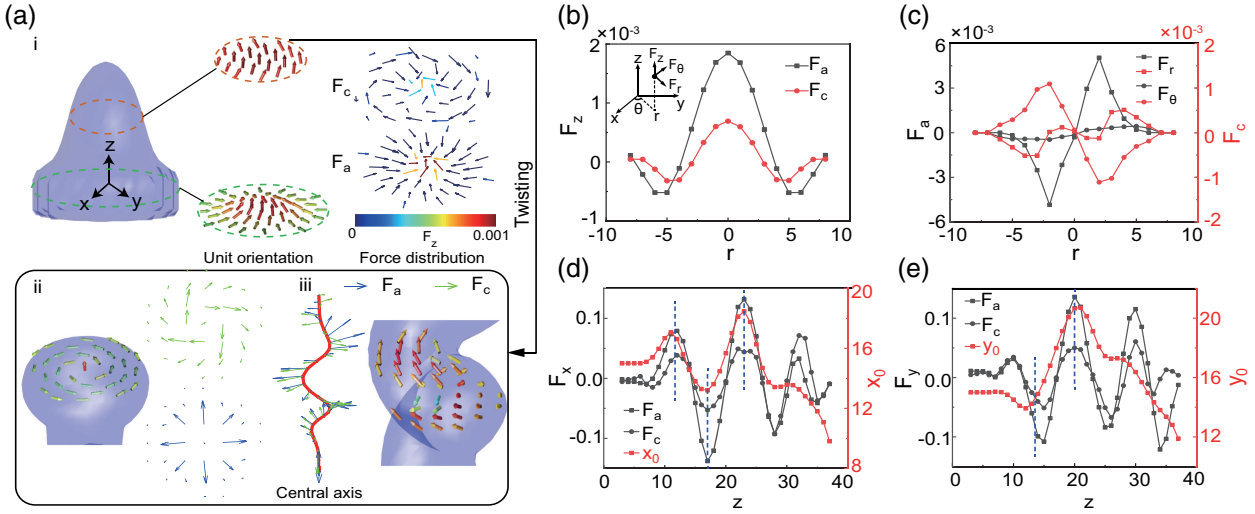

FIG. 4. Active forces and unit orientation during 3D tissue morphogenesis. (a) Unit orientation and active forces corresponding to the initial stage in state (i), tip spheroidization in state (ii), and spiralization in state (iii). The height of the planes corresponding to the active force fields is 4 (i) and 24 (ii), respectively. (b) The z components of $\mathbf{F}_a$ and $\mathbf{F}_c$ with respect to the radial coordinate r, where $\zeta_a = \zeta_c = 0.006$. (c) The radial ($F_r$) and circumferential ($F_\theta$) components of $\mathbf{F}_a$ and $\mathbf{F}_c$ with respect to r, where $\zeta_a = \zeta_c = 0.006$. (d) The x components of $\mathbf{F}_a$ and $\mathbf{F}_c$, and the central axis x_0 versus z, where $\zeta_a = 0.008$ and $\zeta_c = 0.009$. The blue dashed line indicates their common extremum. (e) The y components of $\mathbf{F}_a$ and $\mathbf{F}_c$, and the central axis y_0 versus z.

at the bud tip, inducing the spheroidization in state (ii) [Fig. 4(a)]. For $\mathbf{F}_c$, the larger circumferential component F_θ compared with the radial one indicates that the distribution of $\mathbf{F}_c$ is rotating spiral (clockwise). Interestingly, our simulation shows that cells at the distal end may undergo collective rotation driven by $\mathbf{F}_c$ during spheroidization [Fig. S8] (Movies S9 and S10) [39] and thus exhibit dynamical chirality, although this state displays overall axisymmetrical geometry. Similar collective rotation was also observed in the self-organization of myoblasts [43] and during alveologenesis of human mammary gland organoids [58].

On the other hand, the twisting results in the torsion of units between the different layers in the vertical direction, which leads to state (iii) in Fig. 4(a). By calculating the active forces in each layer, we find that their x (y) components synchronize with the phase of the central axis x_0 (y_0), regardless of whether they are achiral or chiral [Figs. 4(d) and 4(e)] (Movie S11). This indicates that $\mathbf{F}_a$ and $\mathbf{F}_c$ point outward along the radial direction of the helix, which induces corresponding velocity field [Fig. S9] [39], thus driving the formation of the helical structure.

We quantify morphological traits of the emerging structures and probe how physical parameters regulate them. We first characterize the evolution of the radius of the tip spheroid (R) and the helical angle α over time [Fig. S10] [39]. During the structure formation, R gradually increases, while α gradually decreases from 90° over time and finally reaches a saturate helical angle, which reflects the ultimate degree of spiralization. We focus on the magnitude of α and the growth rate $\dot{R}$.

We draw $\dot{R}$ under different activity strength ζ_a and ζ_c, and find that increasing ζ_a and ζ_c can significantly promote the growth of R [Fig. 5(a)]. This indicates that the formation of the tip spheroid requires sufficient achiral and chiral active stresses. We find that under different ζ_c, the growth rate $\dot{R}$ as a function of ζ_a almost collapses to $(\zeta_a - \zeta_{a0})^{0.62}$ [Fig. 5(b)], where the fitting parameter ζ_{a0} corresponds to

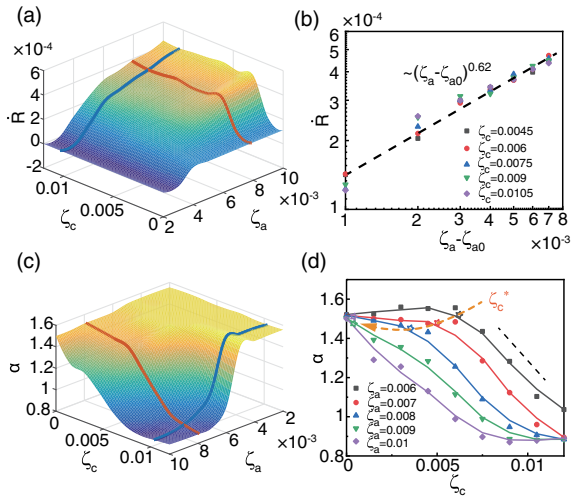

FIG. 5. (a) The growth rate $\dot{R}$ of the tip spheroid as a function of achiral activity ζ_a and chiral activity ζ_c. (b) The dependence of $\dot{R}$ on ζ_a under different ζ_c. The dashed line is the fitting by using $(\zeta_a - \zeta_{a0})^{0.62}$, where $\zeta_{a0} = 0.003$. (c) The spiral angle α as a function of ζ_a and ζ_c. (d) The dependence of α on ζ_c under different ζ_a. The stars at the "shoulder" of the curves indicate the thresholds ζ_c^* for spiralization.

the required achiral activity driving bud growth. If the tip spheroid undergoes isotropic growth, driven by the achiral activity, the growth rate of its radius will be proportional to $\zeta_a - \zeta_{a0}$. However, our simulations show that the exponential of the scaling law (0.62) is less than 1, revealing anisotropic growth in the simulated spheroid. Such a behavior may be attributed to the vortexlike polarization field that displays nonspherical symmetry.

Increasing ζ_a and ζ_c can significantly promote spiralization (decreasing helix angle α) of the tentacle [Fig. 5(c)]. Under different achiral strength ζ_a, the helix angle α exhibits distinct trends with respect to ζ_c [Fig. 5(d)]. There exists a critical chiral activity ζ_c^*, beyond which the cylindrical frenulum begins to spiralize. The ζ_c^* for triggering such spiralization can be significantly reduced by increasing ζ_a. This reveals that the achiral active stress contributes to overcoming the energy barrier for morphological distortion to initiate subsequent spiralization. After spiralization starts, however, the resistance of the rod-shaped tentacle to twisting, referred to as torsion stiffness, displays less dependence on the achiral active stress, as revealed by the almost constant slope of α with respect to ζ_c in this stage. It indicates that the torsion stiffness of the self-organized tentacle is intrinsic and insensitive to achiral activity. Our experimental measurement shows $\dot{R} = 0.511 \pm 0.246$ μm/h and $\alpha = 0.883 \pm 0.113$ $(n = 8)$, which is consistent with the ranges of the growth rate 0–0.706 μm/h and the helix angle 0.870–1.571 predicted by our theory.

In summary, we have theoretically explored 3D chiral morphogenesis of soft tissues. We demonstrate that the cellular level handedness can be translated to tissue level to generate papillary and helical structures, which have been observed in experiments of ours and other groups [42,43]. The chirality transmission and the emerging 3D morphodynamics are revealed to be governed by the coordination between the chiral and achiral active stresses. Although described phenomenologically in our theory, these active stresses naturally result from the molecular configurations, cytoskeleton arrangements, intracellular flows, and intercellular adhesion [26–29]. Our work highlights the essential role of mechanical forces in sculpting living tissues.

Supports from National Natural Science Foundation of China (Grants No. 12325209, No. 12272202, and No. 11921002) are acknowledged.

*These authors contributed equally to this work.
†Corresponding author: libome@tsinghua.edu.cn

[1] W. T. D'Arcy, *On Growth and Form* (Cambridge University Press, Cambridge, England, 1942).
[2] E. Hannezo and C. P. Heisenberg, Cell **178**, 12 (2019).
[3] V. Shankar, C. van Blitterswijk, E. Vrij, and S. Giselbrecht, Adv. Sci. **8**, 2004250 (2021).
[4] M. Valet, E. D. Siggia, and A. H. Brivanlou, Nat. Rev. Mol. Cell Biol. **23**, 169 (2022).
[5] J. Ackermann, P. J. R. Cohen, K. Alessandri, A. Leonard, P. Nassoy, J. F. Joanny, and M. Ben Amar, J. Mech. Phys. Solids **160**, 104778 (2022).
[6] R. Alert and X. Trepat, Annu. Rev. Condens. Matter Phys. **11**, 77 (2020).
[7] M. Poujade, E. Grasland-Mongrain, A. Hertzog, J. Jouanneau, P. Chavrier, B. Ladoux, A. Buguin, and P. Silberzan, Proc. Natl. Acad. Sci. U.S.A. **104**, 15988 (2007).
[8] M. C. Marchetti, J. F. Joanny, S. Ramaswamy, T. B. Liverpool, J. Prost, M. Rao, and R. A. Simha, Rev. Mod. Phys. **85**, 1143 (2013).
[9] S. Ramaswamy, Annu. Rev. Condens. Matter Phys. **1**, 323 (2010).
[10] A. Doostmohammadi, J. Ignés-Mullol, J. M. Yeomans, and F. Sagués, Nat. Commun. **9**, 3246 (2018).
[11] R. Zhang, A. Mozaffari, and J. J. de Pablo, Nat. Rev. Mater. **6**, 437 (2021).
[12] M. J. Bowick, N. Fakhri, M. C. Marchetti, and S. Ramaswamy, Phys. Rev. X **12**, 010501 (2022).
[13] É. Fodor, R. L. Jack, and M. E. Cates, Annu. Rev. Condens. Matter Phys. **13**, 215 (2022).
[14] J. Ackermann, M. Ben Amar, and J. F. Joanny, Phys. Rep. **927**, 1 (2021).
[15] S. Shankar, A. Souslov, M. J. Bowick, M. C. Marchetti, and V. Vitelli, Nat. Rev. Phys. **4**, 380 (2022).
[16] M. R. Nejad and J. M. Yeomans, Phys. Rev. Lett. **128**, 048001 (2022).
[17] R. Hartmann, P. K. Singh, P. Pearce, R. Mok, B. Song, F. Díaz-Pascual, J. Dunkel, and K. Drescher, Nat. Phys. **15**, 251 (2019).
[18] L. A. Hoffmann, L. N. Carenza, J. Eckert, and L. Giomi, Sci. Adv. **8**, eabk2712 (2022).
[19] L. Metselaar, J. M. Yeomans, and A. Doostmohammadi, Phys. Rev. Lett. **123**, 208001 (2019).
[20] L. J. Ruske and J. M. Yeomans, Phys. Rev. X **11**, 021001 (2021).
[21] J.-B. Coutelis, N. González-Morales, C. Géminard, and S. Noselli, EMBO Rep. **15**, 926 (2014).
[22] S. Nonaka, Y. Tanaka, Y. Okada, S. Takeda, A. Harada, Y. Kanai, M. Kido, and N. Hirokawa, Cell **95**, 829 (1998).
[23] M. Hashimoto, K. Shinohara, J. Wang, S. Ikeuchi, S. Yoshiba, C. Meno, S. Nonaka, S. Takada, K. Hatta, A. Wynshaw-Boris, and H. Hamada, Nat. Cell Biol. **12**, 170 (2010).
[24] C. Weaver and D. Kimelman, Development (Cambridge, U.K.) **131**, 3491 (2004).
[25] S. Yin, B. Li, and X. Q. Feng, Proc. Natl. Acad. Sci. U.S.A. **119**, e2206159119 (2022).
[26] S. R. Naganathan, S. Fürthauer, M. Nishikawa, F. Jülicher, and S. W. Grill, eLife **3**, e04165 (2014).
[27] S. R. Naganathan, T. C. Middelkoop, S. Fürthauer, and S. W. Grill, Curr. Opin. Cell Biol. **38**, 24 (2016).
[28] Y. H. Tee, T. Shemesh, V. Thiagarajan, R. F. Hariadi, K. L. Anderson, C. Page, N. Volkmann, D. Hanein, S. Sivaramakrishnan, M. M. Kozlov, and A. D. Bershadsky, Nat. Cell Biol. **17**, 445 (2015).

[29] F. J. Segerer, F. Thüroff, A. Piera Alberola, E. Frey, and J. O. Rädler, Phys. Rev. Lett. **114**, 228102 (2015).
[30] A. S. Chin, K. E. Worley, P. Ray, G. Kaur, J. Fan, and L. Q. Wan, Proc. Natl. Acad. Sci. U.S.A. **115**, 12188 (2018).
[31] L. Yamauchi, T. Hayata, M. Uwamichi, T. Ozaway, and K. Kawaguchi, arXiv:2008.10852v1.
[32] K. Sato, T. Hiraiwa, E. Maekawa, A. Isomura, T. Shibata, and E. Kuranaga, Nat. Commun. **6**, 10074 (2015).
[33] G. Duclos, C. Blanch-Mercader, V. Yashunsky, G. Salbreux, J. F. Joanny, J. Prost, and P. Silberzan, Nat. Phys. **14**, 728 (2018).
[34] L. A. Hoffmann, K. Schakenraad, R. M. H. Merks, and L. Giomi, Soft Matter **16**, 764 (2020).
[35] V. Yashunsky, D. J. G. Pearce, C. Blanch-Mercader, F. Ascione, P. Silberzan, and L. Giomi, Phys. Rev. X **12**, 041017 (2022).
[36] Z. Y. Li, D. Q. Zhang, S. Z. Lin, and B. Li, Phys. Rev. Lett. **125**, 098002 (2020).
[37] S. Nasr Esfahani, Y. Shao, A. M. Resto Irizarry, Z. Li, X. Xue, D. L. Gumucio, and J. Fu, Biomaterials **216**, 119244 (2019).
[38] F. Lin, X. Li, S. Sun, Z. Y. Li, C. Lv, J. Bai, L. Song, Y. Han, B. Li, J. Fu, and Y. Shao, Nat. Commun. **14**, 6016 (2023).
[39] See Supplemental Material at http://link.aps.org/supplemental/10.1103/PhysRevLett.132.138401 for details of theoretical model, numerical method, and additional results.
[40] S. Lo Vecchio, O. Pertz, M. Szopos, L. Navoret, and D. Riveline, Nat. Phys. **20**, 322 (2024).
[41] L. Giomi and M. C. Marchetti, Soft Matter **8**, 129 (2012).
[42] C. Blanch-Mercader, P. Guillamat, A. Roux, and K. Kruse, Phys. Rev. Lett. **126**, 028101 (2021).
[43] P. Guillamat, C. Blanch-Mercader, G. Pernollet, K. Kruse, and A. Roux, Nat. Mater. **21**, 588 (2022).
[44] F. Caballero and M. C. Marchetti, Phys. Rev. Lett. **129**, 268002 (2022).
[45] M. E. Cates and E. Tjhung, J. Fluid Mech. **836**, P1 (2018).
[46] T. B. Saw, A. Doostmohammadi, V. Nier, L. Kocgozlu, S. Thampi, Y. Toyama, P. Marcq, C. T. Lim, J. M. Yeomans, and B. Ladoux, Nature (London) **544**, 212 (2017).
[47] L. Balasubramaniam, A. Doostmohammadi, T. B. Saw, G. H. N. S. Narayana, R. Mueller, T. Dang, M. Thomas, S. Gupta, S. Sonam, A. S. Yap, Y. Toyama, R.-M. Mége, J. M. Yeomans, and B. Ladoux, Nat. Mater. **20**, 1156 (2021).
[48] D. Q. Zhang, P. C. Chen, Z. Y. Li, R. Zhang, and B. Li, Proc. Natl. Acad. Sci. U.S.A. **119**, e2122494119 (2022).
[49] S. Fürthauer, M. Strempel, S. W. Grill, and F. Jülicher, Phys. Rev. Lett. **110**, 048103 (2013).
[50] T. Markovich, E. Tjhung, and M. E. Cates, New J. Phys. **21**, 112001 (2019).
[51] L. N. Carenza, G. Gonnella, D. Marenduzzo, and G. Negro, Proc. Natl. Acad. Sci. U.S.A. **116**, 22065 (2019).
[52] E. Tjhung, M. E. Cates, and D. Marenduzzo, Proc. Natl. Acad. Sci. U.S.A. **114**, 4631 (2017).
[53] A. Doostmohammadi, M. F. Adamer, S. P. Thampi, and J. M. Yeomans, Nat. Commun. **7**, 10557 (2016).
[54] R. Zhang, T. Roberts, I. S. Aranson, and J. J. de Pablo, J. Chem. Phys. **144**, 084905 (2016).
[55] M. E. Cates, K. Stratford, R. Adhikari, P. Stansell, J. C. Desplat, I. Pagonabarraga, and A. J. Wagner, J. Phys. Condens. Matter **16**, S3903 (2004).
[56] Y. Maroudas-Sacks, L. Garion, L. Shani-Zerbib, A. Livshits, E. Braun, and K. Keren, Nat. Phys. **17**, 251 (2021).
[57] Z. Wang, M. C. Marchetti, and F. Brauns, Proc. Natl. Acad. Sci. U.S.A. **120**, e2220167120 (2023).
[58] P. A. Fernández, B. Buchmann, A. Goychuk, L. K. Engelbrecht, M. K. Raich, C. H. Scheel, E. Frey, and A. R. Bausch, Nat. Phys. **17**, 1130 (2021).
[59] F. Vafa and L. Mahadevan, Phys. Rev. Lett. **129**, 098102 (2022).
[60] M. Ravnik and J. M. Yeomans, Phys. Rev. Lett. **110**, 026001 (2013).
[61] T. Markovich and T. C. Lubensky, Phys. Rev. Lett. **127**, 048001 (2021).